Journal of Nanobiotechnology

RESEARCH

Open Access

Magnesium metal–organic framework microneedles loaded with curcumin for accelerating oral ulcer healing

Junhui Liu[1,2], Zhipeng Zhang[3], Xiufei Lin[2], Jun Hu[2], Xiaoyi Pan[2], Anqi Jin[1], Lanjie Lei[1*] and Minghai Dai[2*]

Abstract

Oral ulcers are a common oral mucosal disease that seriously affect the quality of life. Traditional drug treatments have shown unsatisfactory efficacy and potential adverse reactions. In this study, curcumin-loaded multifunctional magnesium metal–organic framework-embedded hyaluronic acid-soluble microneedles patches were developed to optimize treatment strategies for oral ulcers. This microneedles patch achieves efficient release of curcumin and Mg^{2+} in the ulcer through precisely targeted delivery and controllable release mechanism, significantly regulates inflammation, promotes cell migration and angiogenesis, and accelerates the ulcer healing process. At the same time, the synergistic effect of curcumin and gallic acid effectively alleviated oxidative stress, while the backplate ε-poly-L-lysine and needle tip Mg^{2+} jointly constructed an antibacterial barrier to effectively inhibit pathogens. Verification using an oral ulcer rat model showed that the microneedles patch exhibited excellent therapeutic effects. This not only opens up a new avenue for clinical oral treatment but also marks a breakthrough in nanobiomaterials science and drug delivery technology and heralds a broad prospect in the field of oral ulcer treatment in the future.

Keywords Oral ulcer, Microneedles, Curcumin, Metal-organic framework, ε-Poly-L-lysine

*Correspondence:
Lanjie Lei
leilanjie1988@163.com
Minghai Dai
meanhy@wmu.edu.cn
Full list of author information is available at the end of the article

Graphical Abstract

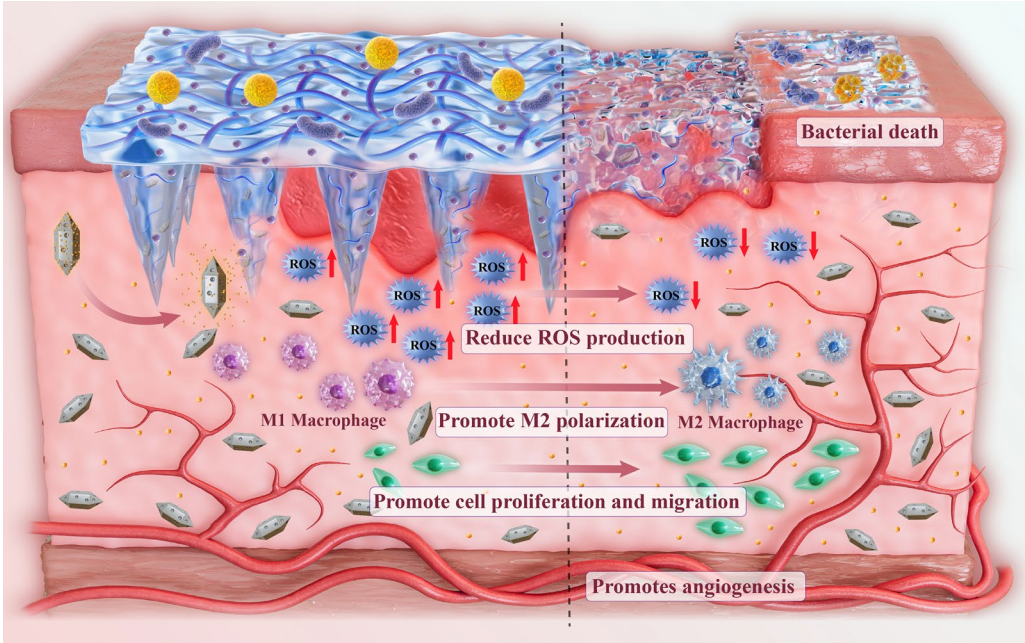

Introduction

As ubiquitous oral mucosal lesions, oral ulcers have a clinical attack rate as high as 20% and have a significant negative impact on patients' quality of life [1], which is mainly attributed to their inherent tendency to relapse and the accompanying severe pain experience [2]. Pathologically, the condition is characterized by the loss of mucosal epithelial continuity and marked inflammatory cell infiltration at the ulcer base [3]. For cases with frequent recurrences and complex situations, traditional treatments such as hormones, transfer factors, and immunomodulators have certain therapeutic effects, but are often accompanied by a series of adverse reactions such as immune dysfunction, disruption of oral microecological balance, increased risk of wound infection, and allergic reactions [3–7]. In addition, existing drug delivery methods, including local injection and direct mucosal administration, have certain limitations [8, 9]. Commercial oral ulcer dressings also face challenges in terms of drug absorption efficiency, distribution uniformity, and drug efficacy stability when dealing with complex and changing microenvironments in the oral cavity [10–12]. In view of this, to further optimize the clinical treatment effects of oral ulcers and reduce the side effects of treatment, it is urgent to deeply explore and innovatively develop more efficient and safe new treatment strategies.

Natural biomaterials are increasingly becoming the focus of scientific research because of their wide availability, excellent biological activity, significant therapeutic benefits, and biodegradability. Among them, curcumin (CUR), as a hydrophobic polyphenolic compound derived from turmeric, is known as the "golden molecule" for its multiple effects of regulating inflammatory responses, alleviating oxidative stress, and inhibiting tumor growth [13–18]. CUR has shown great potential in the treatment of oral and systemic diseases [19–21]. Compared with hormonal drugs, CUR avoids side effects owing to its excellent safety and promotes the healing of oral ulcers in multiple dimensions through multiple biological effects. However, the clinical application of CUR is limited by its inherent low water solubility and physicochemical instability, which directly affects its bioavailability and in vivo stability [22]. To overcome the bottleneck of drug efficacy and dosage optimization, research has focused on encapsulating CUR in nanoparticles with high drug loading, controlled release, and bioprotection properties [23–26]. Porous magnesium metal–organic framework (Mg-MOF) are considered ideal drug delivery carriers because they can slowly degrade in the body and release magnesium and gallic acid, regulate cell function, and accelerate wound healing [27, 28]. Although research on metal–organic framework (MOF) is progressing rapidly, their potential in the treatment of oral diseases is yet to be fully explored and verified.

Microneedles (MNs), as an emerging drug delivery system, have shown broad application prospects due to

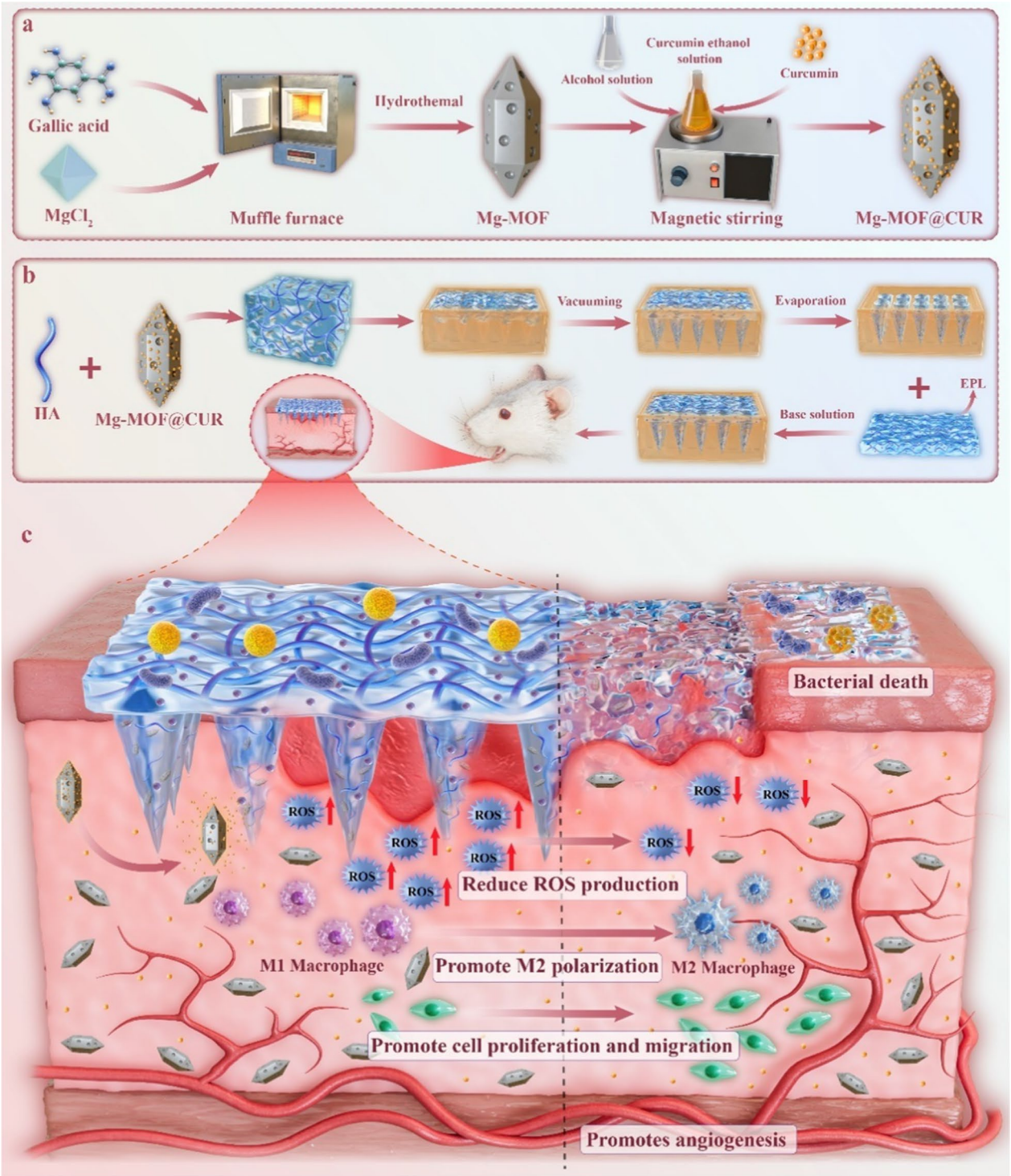

Fig. 1 Schematic diagram of multifunctional soluble microneedles (denoted as HEMC-MNs) for the treatment of oral ulcers. **a** Schematic diagram illustrating the process of synthesizing CUR-loaded Mg-MOF. **b** Schematic illustration depicting the process of preparing HEMC MNs; **c** schematic depiction illustrating the utilization of HEMC MNs to promote oral ulcer healing

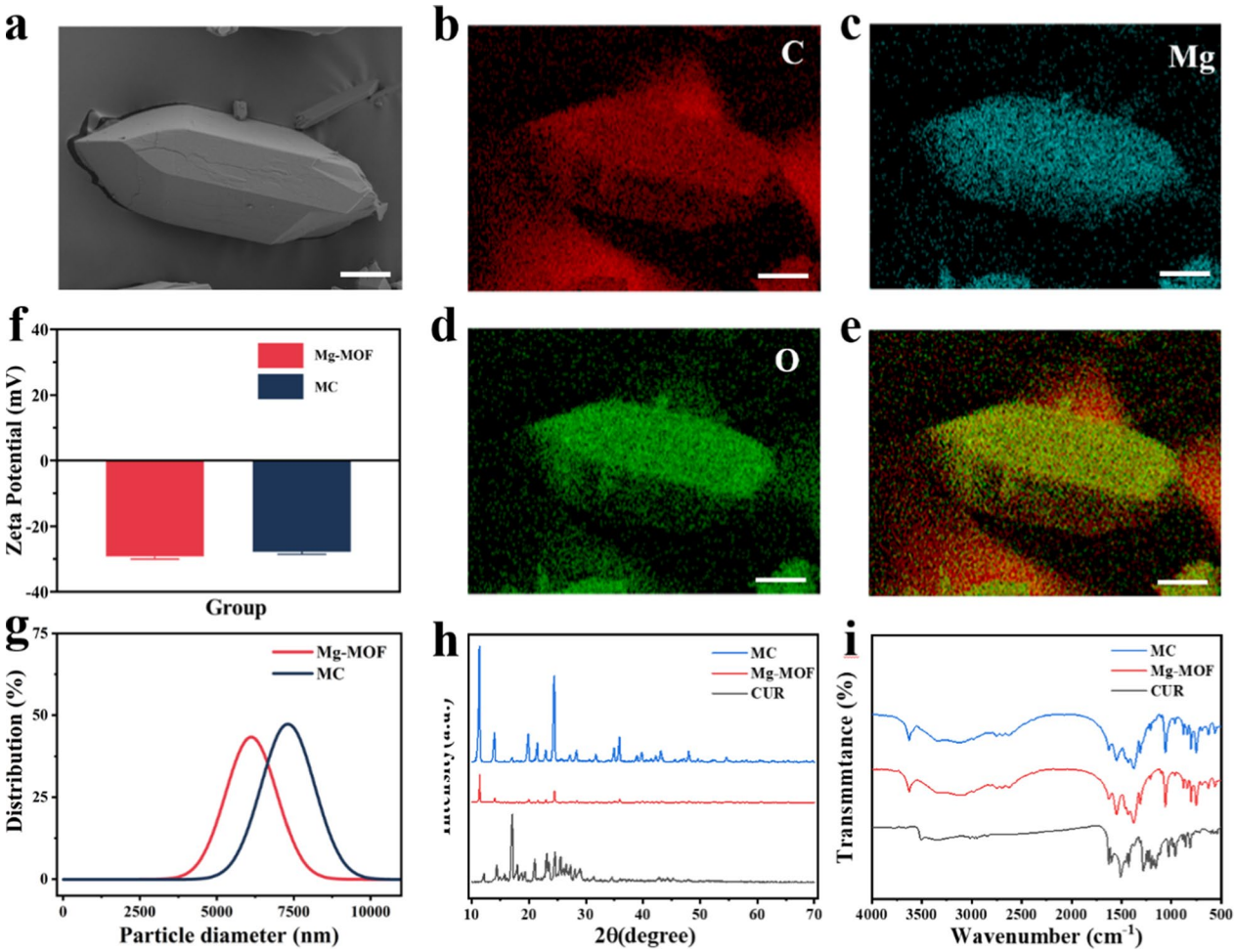

Fig. 2 Synthesis and characterization of Mg-MOF and MC. **a** SEM image of MC. Scale bars: 1 μm. **b**–**e** Elemental distribution images of MC. Scale bars: 1 μm. **f** Zeta potential of Mg-MOF and MC. **g** Size distribution of Mg-MOF and MC nanoparticles. **h** FT-IR spectra of CUR, Mg-MOF and MC. **i** XRD patterns of CUR, Mg-MOF and MC

their minimally invasive, painless and easy operation [29, 30]. Its structural features lie in the array arrangement of micron-sized pointed protrusions. This design enables it to penetrate the mucosal epithelium and lamina propria, construct a temporary delivery channel, effectively circumvent the mucosal barrier, and achieve the efficient delivery of drugs directly targeted to the lesion area. Compared to traditional oral dressings and hydrogel systems, this mechanism significantly improves the efficiency and accuracy of drug delivery [31]. Recent scientific research has focused on the application of MNs arrays in the field of oral disease treatment [32]. However, current MNs drug delivery systems are limited to steroids and immunomodulators. Although effective, they are associated with a risk of adverse events. In addition, they have a narrow therapeutic range and require frequent administration, which limits their ability to release drugs in a sustained and stable manner, thereby becoming a bottleneck in the widespread application of MNs technology [33, 34]. Therefore, the development of more efficient, safe, and adaptable MNs systems to broaden the therapeutic range, reduce the frequency of administration, and improve patient compliance has become an important issue that needs to be urgently addressed in the current scientific research field.

In this study, we developed a multifunctional MNs patch with CUR-loaded Mg-MOF for accelerated oral ulcer healing (Fig. 1). The Mg-MOF framework prepared by the hydrothermal method was efficiently loaded with the natural biomaterial CUR using ultrasonic adsorption technology. Then, a composite strategy of molecular-level blending and matrix embedding was adopted to successfully disperse the MC composite nanoparticles uniformly and firmly embed them into the hyaluronic acid (HA) matrix to construct the precisely released MNs tip. MNs achieve the synergistic delivery of CUR, Mg^{2+},

and gallic acid in ulcer lesions, effectively exerting anti-inflammatory and pro-angiogenic effects and reducing oxidative stress and tissue damage. In addition, the EPL/HA complex on the back layer of the MNs synergistically exhibited antibacterial properties with Mg^{2+}, further consolidating the therapeutic effect. This multifunctional MNs patch is the first innovative attempt to use MOF as a carrier to deliver natural bioactive molecules to the oral mucosa. It not only expands the application scope of MOF in the biomedical field, but also sets a new scientific benchmark for the noninvasive treatment of oral mucosal diseases and provides a solid experimental foundation and theoretical support.

Results and discussion

Syntheses and characterizations of the MC

Mg-MOFs were synthesized using a hydrothermal technique [35]. Examination of the morphology of MC using scanning electron microscopy (SEM) indicated a uniform bipyramidal structure with discernible CUR particles

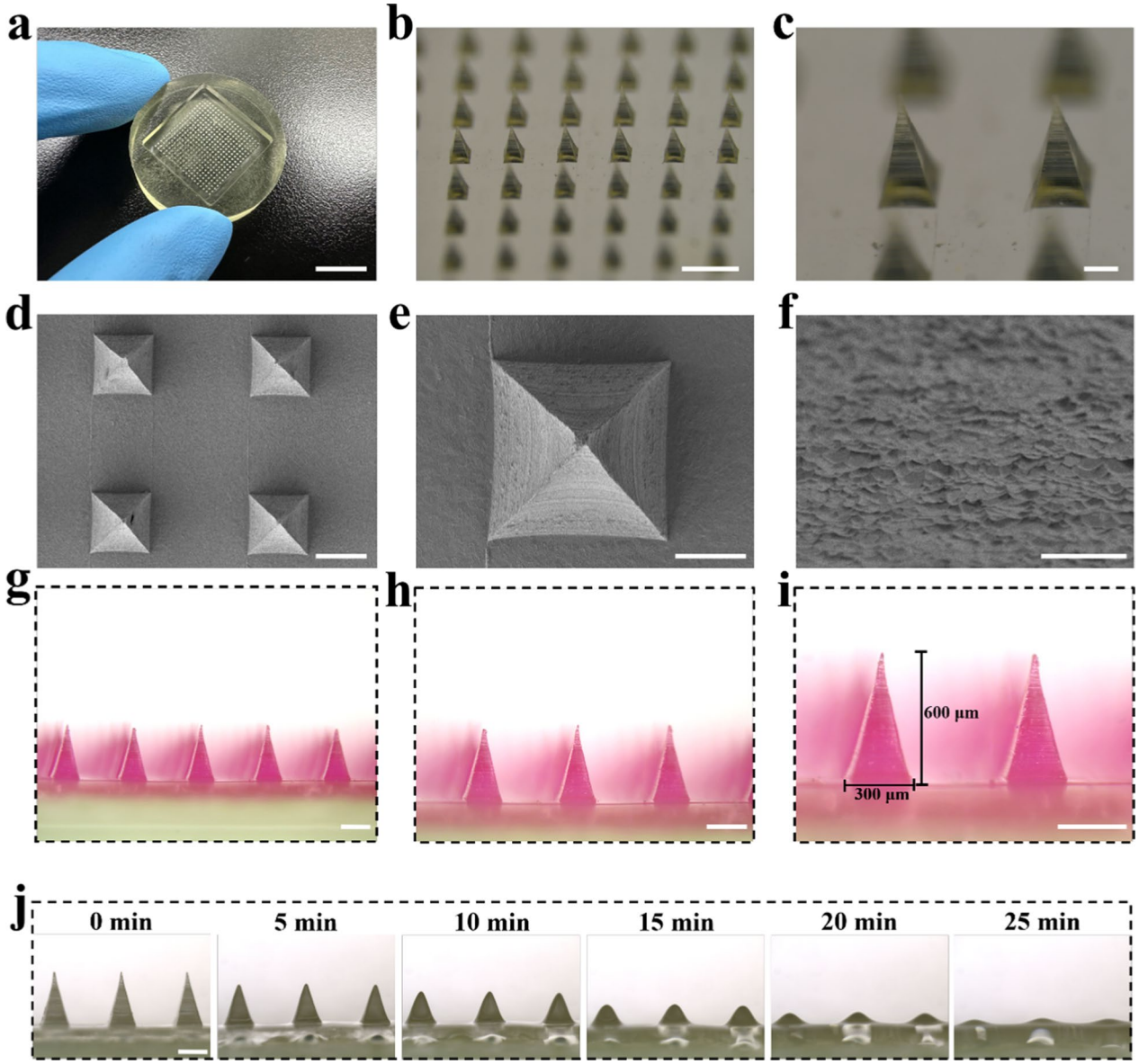

Fig. 3 Synthesis and characterization of HEMC MNs. **a** Digital photographs of PDMS MNs moulds. **b**, **c** Light microscopy images of HEMC MNs. **d**–**f** SEM images of HEMC MNs. **g**–**i** Stereomicroscope images of HEMC MNs after Rhodamine B staining. The labels indicate the specific dimensions of the MNs tip: 300 μm diameter at the base and 600 μm height. **j** Stereomicroscope images of HEMC MNs after moisture uptake at different time points in a 75% humidity chamber

present on the surface (Fig. 2a). Elemental distribution analysis using bright-field scanning SEM confirmed the uniform distribution of C, O, and Mg within the MC nanoparticles (Fig. 2b–e). Additionally, scanning the MC using energy-dispersive spectroscopy (EDS) showed the same elemental distribution (Figure S1a, b). The zeta potentials of Mg-MOF, CUR, and MC were analyzed to assess the changes in the surface charge of the MC. The zeta potential of Mg-MOF was −29.17 mV, while that of MC was −27.8 mV, indicating that loading CUR did not affect the stability of Mg-MOF (Fig. 2f).

Laser particle size analysis showed that the average particle size of the prepared Mg-MOF particles was approximately 6 μm. After loading with CUR, the particle size of the MC composite increased slightly to the range of 7.5 μm (Fig. 2g). The X-ray diffraction (XRD) spectrum confirmed that Mg-MOF crystals with excellent morphology were synthesized, which is consistent with existing research results (Fig. 2h) [36]. The XRD characteristic peaks of CUR and Mg-MOF were retained and matched in the MC spectrum, which strongly proves that CUR was successfully loaded.

The Fourier-transform infrared (FT-IR) spectrum of Mg-MOF exhibited distinctive peaks at 1377 and 1550 cm^{-1}, which were attributed to the symmetric and asymmetric stretching C–O vibrations, respectively, of the carboxylic acid group (OCO–). The alteration in the FT-IR spectrum of MC indicated the presence of CUR in Mg-MOF. Following CUR encapsulation, the peak intensities at 988, 1160, and 1235 cm^{-1} increased, exhibiting slight positional changes (Fig. 2i). These results indicate that CUR was effectively encapsulated within the pores of the Mg-MOF. In addition, the absorption spectrum of Mg-MOF exhibited a distinct peak at 273 nm (Figure S2a). According to the standard curve of CUR (Figure S2b), the drug-loading capacity of MC was 23.1%, while its efficiency was found to be 15% using a UV spectrophotometer. In summary, we explored for the first time the use of Mg-MOFs as carriers to achieve gentle encapsulation of CUR through ultrasound-assisted technology, which is significantly different from the previous one-pot loading method that focused on copper-based and zinc-based MOFs. This method effectively avoids the challenge of easy degradation or inactivation of CUR under traditional high-temperature and high-pressure conditions and opens up new avenues for the application of CUR in the fields of biomedicine and materials science.

Synthesis and characterization of HEMC MNs

To improve the efficiency and effectiveness of drug delivery for ulcer healing, HA MNs patches were used to encapsulate MC and EPL, resulting in HA@EPL&Mg-MOF@CUR (HEMC) MNs patches. The HEMC MNs were fabricated via two-step template replication. First, the HEMC MNs patches were prepared using polydimethylsiloxane (PDMS) MNs molds (Fig. 3a). Figure 3b, c depicts the stereomicroscopic image of the MNs patch comprising a 20×20 array of MNs. Each MNs had a quadrangular pyramidal shape. Moreover, SEM revealed that the tips of the HEMC MNs exhibited a pyramidal shape and were arranged systematically on the substrate (Fig. 3d–f). This sharp pyramidal structure enables the rapid, noninvasive, and precise insertion of HEMC MNs into the oral mucosa. The HEMC MNs were then stained with rhodamine B, and the MC-loaded tip and EPL-loaded backing layer measured 600 μm in height and 300 μm in base diameter (Fig. 3g–i). The bioactivity and biodegradability of the HEMC MNs were assessed by evaluating their hygroscopicity. The HEMC MNs patch was placed in a sealed jar at 75% humidity, and morphological changes in the MNs were recorded (Fig. 3j). After 25 min in a humidity chamber, the tips of the MNs exhibited gradual moisture absorption and dissolution. Furthermore, in an in vivo experiment on the oral mucosa of rats, HEMC MNs showed excellent adhesion properties and were able to adhere stably to the surface of the oral mucosa. The microneedle arrays were visible on the ventral mucosa of the tongue, corresponding to the insertion sites of the HEMC MNs (Figure S3a, b). The results showed that the MNs in this study had the strength to penetrate the lamina propria under the epithelium and deliver encapsulated drugs directly into the depth of the ulcer. This finding not only verifies the adaptability and stability of MNs in the oral cavity's high humidity and dynamic physiological environment, but also emphasizes its potential as a drug delivery system for the continuous and effective delivery of therapeutic drugs to the ulcer lesion area.

To detect the release of Mg-MOF and CUR, HEMC-MNs were immersed in phosphate-buffered saline (PBS) to simulate the moist environment of the oral cavity. Ultraviolet–visible (UV–vis) spectroscopy was utilized at wavelengths of 273 and 426 nm to assess the release of Mg-MOF and CUR from HEMC MNs by comparison with their standard curves (Figure S4a, b). The data presented in Figure S4c, d illustrates the release rates of Mg-MOF and CUR from within the HEMC MNs. A controlled-release pattern was observed for both Mg-MOF and CUR. Compared to other Mg-MOF-based therapeutic methods, our HEMC MNs exhibited long-term drug release and higher drug release efficiency. In addition, given that previous studies on oral ulcer treatment have pointed out that the effective retention time of microneedles in the moist and dynamic environment of the oral cavity is a key factor affecting the efficacy, this article particularly emphasizes the long-lasting effect of HEMC

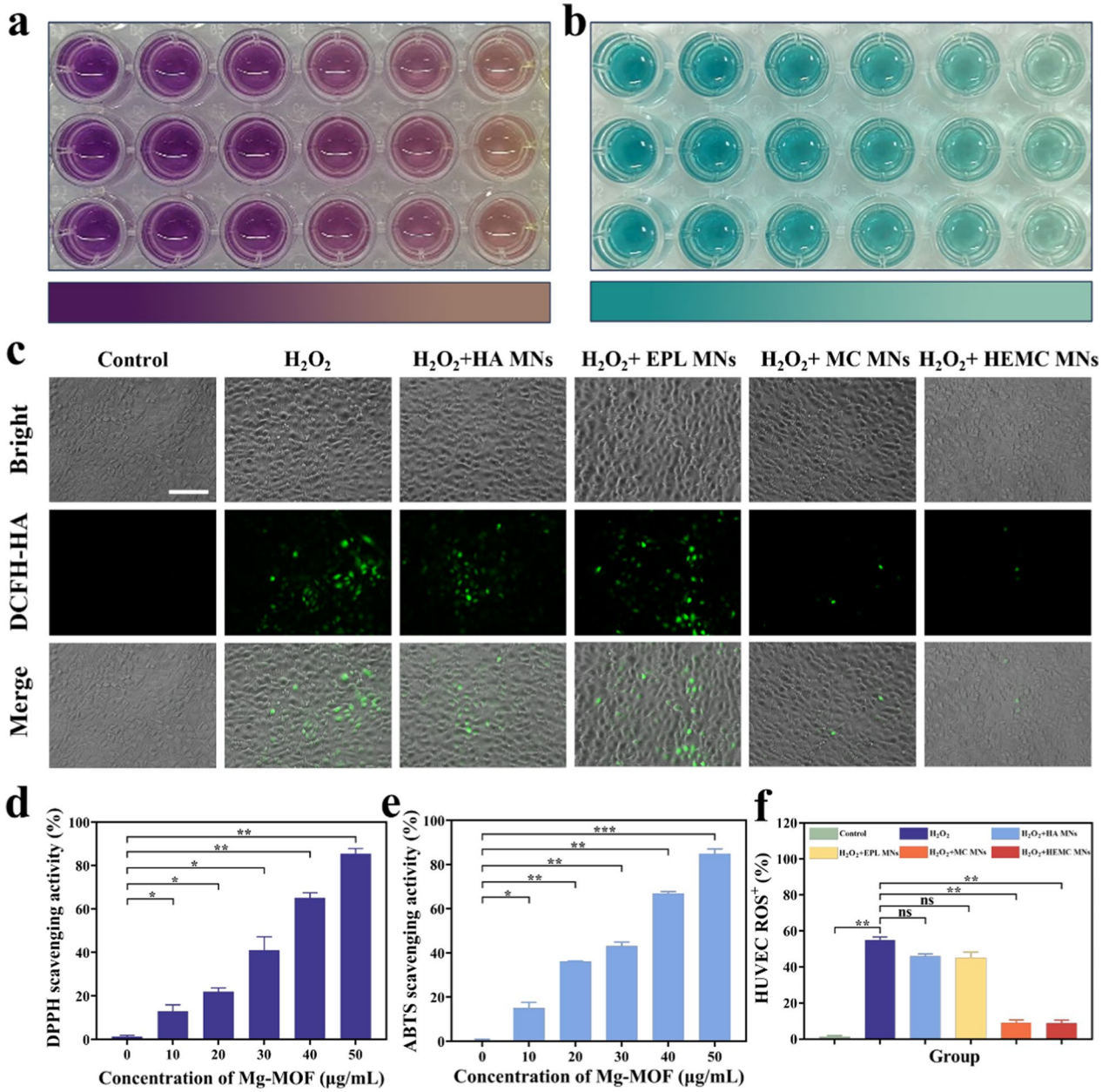

Fig. 4 Evaluation of antioxidant capacity of MC nanoparticles and HEMC MNs. **a** DPPH radical scavenging activity of MC. **b** ABTS scavenging activity of MC. **c** Fluorescence images depicting ROS in HUVEC. Scale bar: 200 μm. **d** Quantitative analysis of DPPH radical scavenging activity of MC. **e** Quantitative analysis of ABTS scavenging activity of MC. **f** Quantitative analysis of ROS levels in HUVEC

MNs in the oral cavity. HEMC MNs can not only release drugs rapidly in the early stage of the disease (within 36 h of the disease) and quickly reach the concentration required for treatment to cope with the rapid progression of oral ulcers, but also its subsequent slow and stable drug release characteristics ensure that the treatment effect can be continuously provided throughout the ulcer healing process, thereby optimizing the treatment effect and accelerating the recovery process.

In addition, we systematically evaluated the wet adhesion properties of HEMC MNs patch and three mainstream commercial oral patches, when applied to oral mucosal tissue. The results showed that the HEMC MNs patch exhibited significantly improved wet adhesion capabilities, with its adhesion strength approximately 1.6 times that of the compared commercial products (Figure S5). This advantage is particularly prominent under the unique humid and dynamic conditions of the

oral environment. This outstanding performance can be attributed to the unique chemical structure of hyaluronic acid molecules in HEMC MNs, whose rich hydroxyl (–OH) and carboxyl (–COOH) functional groups interact with the amino groups (–NH2) and amino groups (–NH2) of mucin molecules on the oral mucosal surface. A solid hydrogen bond network is formed between groups such as hydroxyl groups, which significantly enhances interfacial adhesion. In addition, the interaction between the hydrophobic groups in the hyaluronic acid molecular chain and the hydrophobic regions of mucin, as well as the possible charge attraction effect, jointly promote the tight binding between molecules, especially the increased negative charge density after molecular ionization further strengthens this adhesion mechanism. In summary, HEMC MNs patches, with their optimized wet adhesion properties, can better adapt to the complexity and dynamics of the oral environment compared to the oral mucosal dressings widely used in the current market, ensuring the sustained release and efficient delivery of drugs at the lesion site and providing a solid scientific basis for prolonging the treatment time and improving the treatment effect.

Antioxidant and antibacterial capabilities of HEMC MNs in vitro

Excessive oxidative stress may affect cell repair and prolong healing time [37–39]. In this study, the antioxidant capacities of MC and HEMC MNs were comprehensively and systematically quantitatively evaluated using DPPH and ABTS free radical scavenging assays (Fig. 4a, b). The study found a strong positive correlation between MC concentration and its inhibition efficiency against DPPH free radicals. Especially at a concentration of 50 μg mL^{-1}, MC achieved a high inhibition rate of about 85% (Fig. 4d). This achievement significantly surpasses the antioxidant performance of CUR-loaded poly(L-lactic acid) (PLLA) nanofibrous mesh in the treatment of oral ulcers in the control group and in previous studies, thus highlighting that MC has significant advantages and innovative value in the field of antioxidant treatment [40]. In addition, in the ABTS free radical scavenging test, the addition of MC caused the color of the solution to quickly fade from bright turquoise to colorless, which intuitively reflected its efficient free radical scavenging ability (Fig. 4e). In summary, the Mg-MOF and CUR released by the MC nanoparticles in this study exhibited excellent antioxidant efficacy.

The antioxidant properties of MNs were explored by assessing the oxidative stress status of human umbilical vein endothelial cells (HUVEC) after exposure to MNs of different components. The fluorescent probe 2′,7′-dichlorodihydrofluorescein diacetate (DCFH-DA) was used to accurately monitor dynamic changes in intracellular reactive oxygen species (ROS). By comparing the intensity of the green fluorescence signal, we effectively assessed the ROS levels in HUVEC under different treatment conditions. HUVEC were exposed to 2 mM H_2O_2 to simulate a strong oxidative stress environment as a positive control group, and the results showed significant green fluorescence enhancement (Fig. 4c). Subsequently, compared with the positive control group, the MC MNs and HEMC MNs treatment groups showed significantly reduced expression levels of intracellular ROS (Fig. 4f). This finding strongly proves that HEMC MNs can efficiently scavenge cytotoxic ROS in HUVEC through the synergistic effect of Mg-MOF and CUR released by MC, demonstrating excellent antioxidant properties and potential therapeutic applications.

Antibacterial ability of HEMC MNs in vitro

Oral ulcers are at a high risk of becoming complicated by bacterial infection, which can impair tissue repair and delay the healing process [41–45]. The antibacterial efficacy of the Mg-MOF and EPL components in this study was evaluated through in vitro testing of the MNs against *Staphylococcus aureus* (*S. aureus*) and *Escherichia coli* (*E. coli*). The results of the live-dead bacterial staining experiments showed that as the EPL concentration increased, bacterial activity was significantly inhibited (Figure S6). We then tested the antibacterial effects of different MNs groups. Co-cultures of these bacteria with EPL, MC, or HEMC MNs showed reduced proliferation (Fig. 5a). Conversely, the MNs patch without EPL or MC exhibited no antibacterial effect (Fig. 5d). Live and dead bacterial staining results also revealed that the EPL, MC, and HEMC MNs groups effectively inhibited bacterial growth and efficiently killed bacteria (Fig. 5b, e). The microscopic morphology of the bacteria was examined post-treatment using SEM. *S. aureus* and *E. coli* subjected to EPL, MC, and HEMC MNs displayed abnormal states in morphology and structure when compared to the control group (Fig. 5c). These findings validated the potent inhibitory and bactericidal properties of EPL and MC against *S. aureus* and *E. coli*. Consequently, incorporating MC and EPL into HEMC MNs is expected to aid in the prevention and treatment of bacterial infections that could hinder ulcer healing.

Anti-inflammatory ability of HEMC MNs in vitro

Based on the demonstrated impact of CUR in modulating inflammation and alleviating pain, several studies have established its efficacy in mitigating various manifestations of oral mucosal disorders [46]. Therefore, the regulatory effect of the HEMC MNs patch on the inflammatory state of ulcers was investigated in vitro (Fig. 6a).

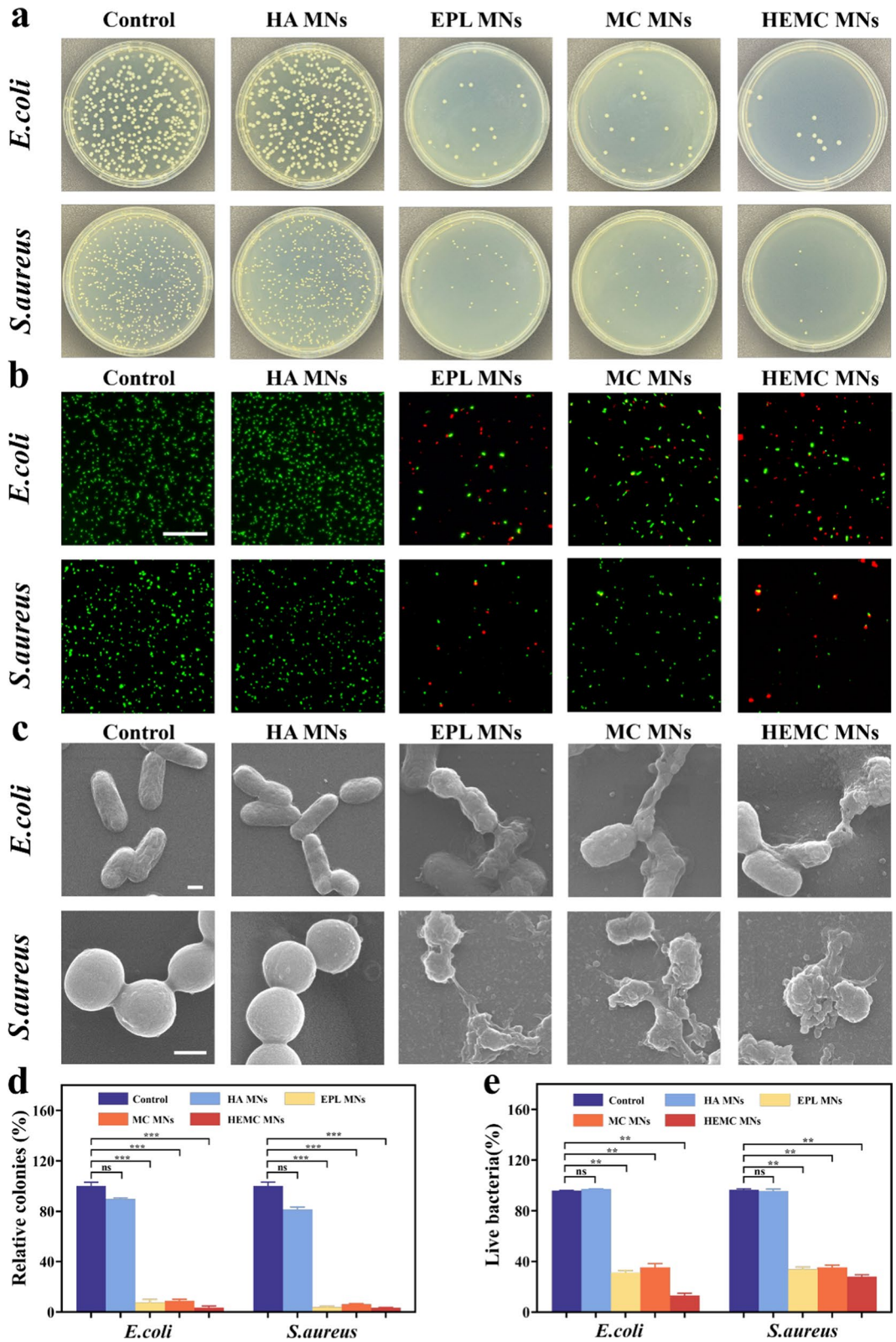

Fig. 5 Detection of antibacterial ability of HEMC MNs. **a** Digital photographs of E. coli and S. aureus colony formation following treatment with different MNs groups. **b** Fluorescence photomicrographs of *E. coli* and *S. aureus* following treatment with different MNs groups. Scale bar: 50 μm. **c** SEM images of *E. coli* and *S. aureus* post-treatment with different MNs. Scale bar: 0.5 μm. **d** Quantitative analysis of colony formation of *E. coli* and *S. aureus*. **e** Quantitative analysis of the viability of *E. coli* and *S. aureus* using live-dead staining

Lipopolysaccharide (LPS) was used to stimulate macrophages in vitro *to* promote an inflammatory state. The cytokine secretion capacity of macrophages was assessed using enzyme-linked immunosorbent assay (ELISA). A decrease in TNF-α and IL-6 levels was observed in macrophages treated with MC MNs and HEMC MNs compared to those in the positive control group (Figure S7a, b). Therefore, the release of CUR from HEMC MNs could effectively inhibit the production of pro-inflammatory molecules by M1 macrophages, inducing anti-inflammatory responses. To confirm the regulatory impact of the HEMC MNs patch on macrophage polarization in vitro, we characterized macrophage polarization using immunofluorescence detection of M1- and M2-type macrophage markers CD86 and CD206. Compared with the control group and other experimental groups, the number of CD86-positive cells in the MC MNs and HEMC MNs treatment groups was significantly reduced (Fig. 6b), while the number of CD206-positive cells was significantly increased (Fig. 6c). This indicates that both MC MNs and HEMC MNs inhibited the M1 phenotype polarization of macrophages and promoted their transformation to M2 macrophages (Fig. 6d, e). Thus, the utilization of HEMC MNs shows promise in mitigating abnormal inflammatory conditions through the facilitation of macrophage polarization toward an anti-inflammatory phenotype, resulting in reduced pro-inflammatory cytokine secretion.

HEMC MNs achieve cell migration and angiogenesis in vitro

An abnormal inflammatory environment impairs cell migration, which results in insufficient mucosal cell adhesion and delayed ulcer healing. According to previous studies, CUR and Mg^{2+} stimulate cell migration and proliferation, thereby promoting angiogenesis and wound healing [27]. To assess the effectiveness of the HEMC MNs in enhancing cell migration, HUVEC migration was examined using an in vitro scratch assay (Fig. 7a). The findings indicated that HUVECs treated with MC and HEMC MNs extracts had higher migration ability compared to that of the control group (Fig. 7d). These results demonstrated that ulcer healing was promoted in vitro using HEMC MNs.

The angiogenic process was also investigated in vitro to evaluate the vascularization activity modulated by the HEMC MNs. There was a notable increase in tube formation in HUVECs following exposure to MC and HEMC MNs compared with that in the control group (Fig. 7b). Significant improvements were also noted in the branch points (Fig. 7e). No obvious effect on tube formation was observed in any of the other groups. In conclusion, we confirmed the capacity of HEMC MNs to enhance cell migration and facilitate blood vessel formation in vitro, suggesting their potential roles in promoting angiogenesis and facilitating ulcer healing in vivo.

Biocompatibility of HEMC MNs patch

Biocompatibility is a critical determinant of the biological utility of the MNs patches. In this study, the biocompatibility of HEMC MNs was assessed using both in vitro and in vivo models. No obvious cytotoxicity of the MC nanoparticles was detected at a concentration of 120 μg mL^{-1} using the CCK-8 detection kit (Figure S8a), suggesting that 120 μg mL^{-1} MC demonstrated appropriate biological safety. In addition, the biocompatibility of EPL was tested. Cell viability decreased, and cell proliferation was inhibited when the concentration reached 400 μg mL^{-1} (Figure S8b). We also used a live-dead cell staining kit to detect cells treated with different MNs extracts. The findings indicated that the growth status and morphology of cells in all experimental groups were normal, with no significant variance observed when compared with the results of the control group (Fig. 7c, f). These findings support the favorable biocompatibility of each type of MNs. The hemolysis test showed that all MNs groups were hemocompatible, as illustrated in Figure S8c-d. The safety of the MNs was assessed in vivo using an oral ulcer rate model on the fifth day following administration. We used hematoxylin and eosin (H&E) staining to investigate organ abnormalities (Figure S9). No changes were observed in rat organs treated with different MNs components, indicating the good biocompatibility of the HEMC MNs patch.

Assessment of MNs in facilitating the healing process of oral ulcers in rat models

We constructed an in vivo oral ulcer rat model to further explore the potential clinical efficacy of the HEMC MNs

(See figure on next page.)

Fig. 6 Detection of anti-inflammatory ability of HEMC MNs. **a** Schematic diagram of HEMC MNs inducing anti-inflammatory polarization of macrophages. Created with BioRender.com. (Agreement number: HF277AO45U). **b** Fluorescence micrographs of DAPI (blue) and CD86 (green) immunofluorescence staining of macrophages. Scale bar: 100 μm. **c** Fluorescence micrographs of DAPI (blue) and CD206 (red) immunofluorescence staining of macrophages. Scale bar: 100 μm. **d** Quantitative analysis of M1-type macrophages expressing CD86. **e** Quantitative analysis of M2-type macrophages expressing CD206

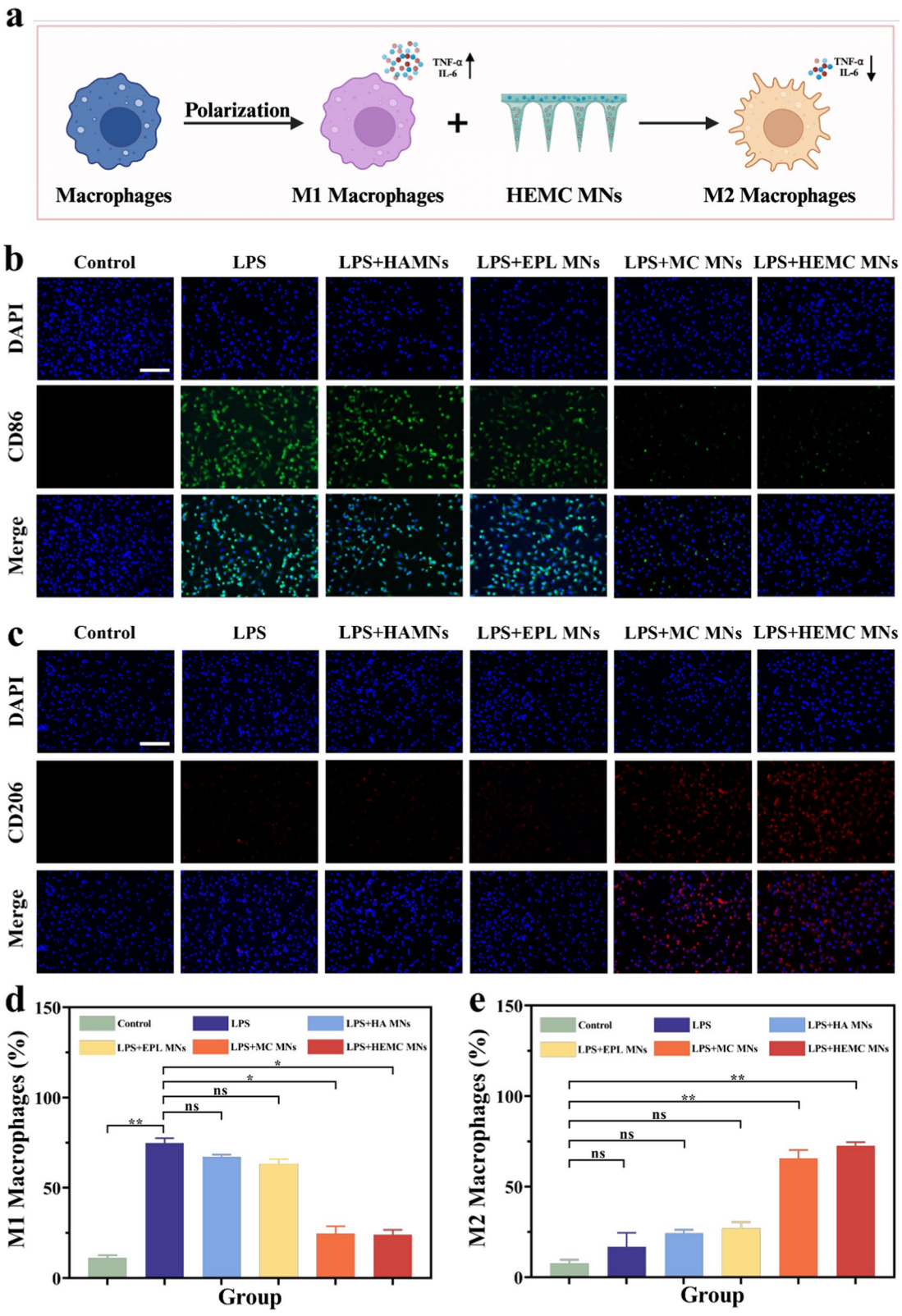

Fig. 6 (See legend on previous page.)

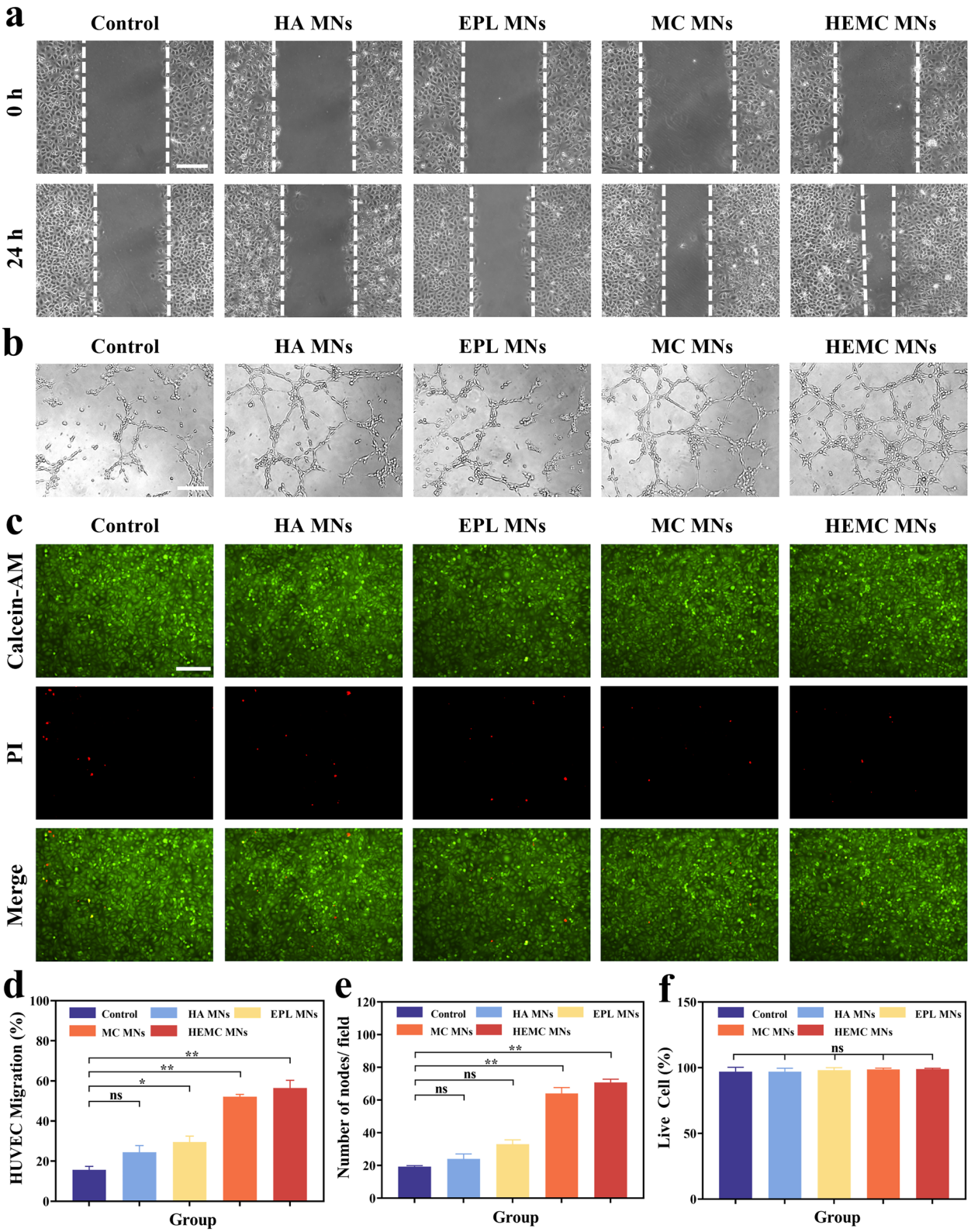

Fig. 7 Angiogenesis, cell migration and biological safety testing. **a** Microscopic images of cell migration in the scratch assay. Scale bar: 250 μm. **b** Tubule formation assay. Scale bar: 250 μm. **c** Fluorescence micrographs of live-dead staining. Scale bar: 250 μm. **d** Quantitative analysis of cell migration in the scratch assay. **e** Quantitative analysis of angiogenesis. **f** Quantitative analysis of live-dead cell staining

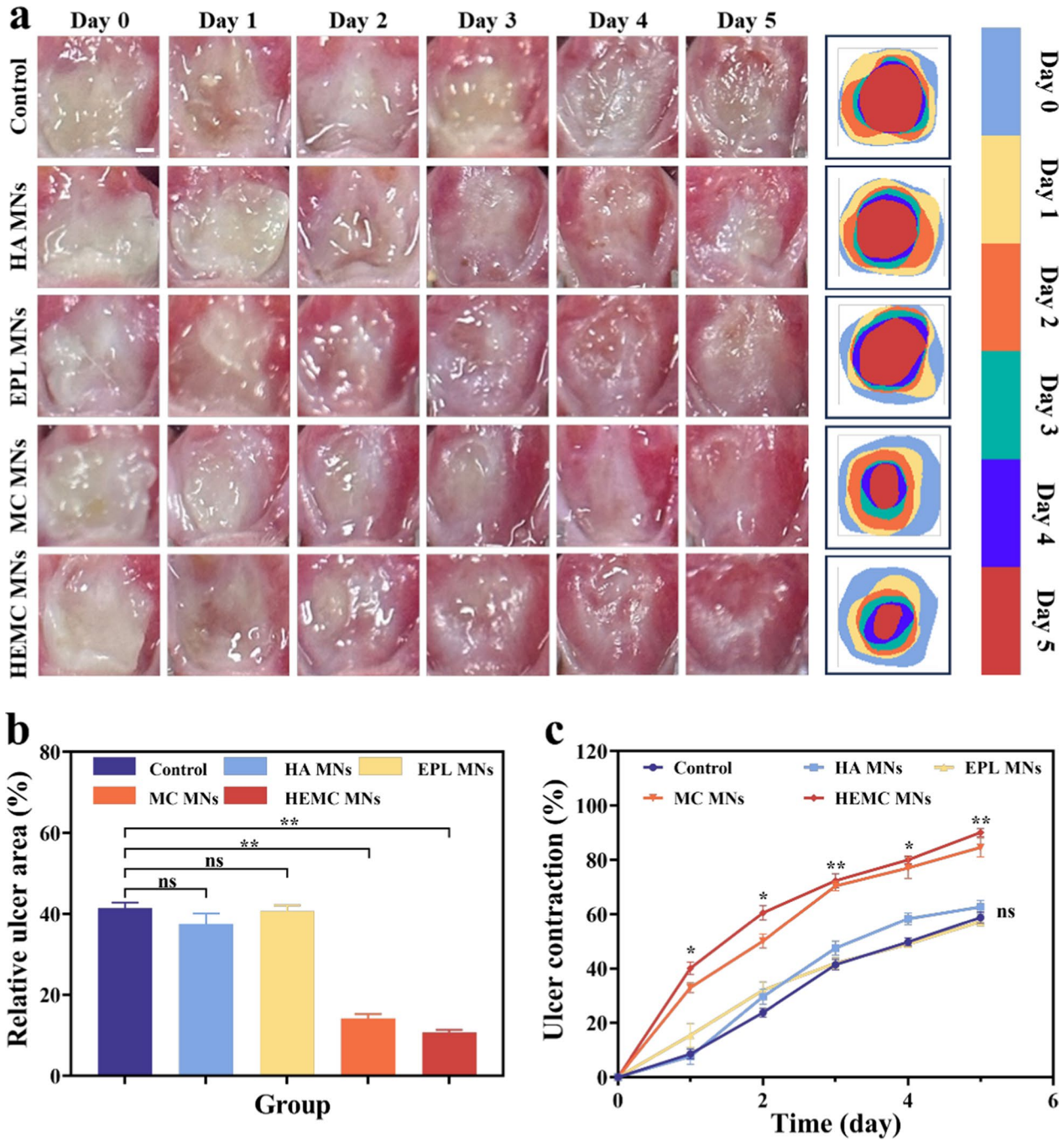

Fig. 8 In vivo ulcer healing assessment in rats with oral ulcers. **a** Digital photographs of ulcer healing in rats following treatment in different MNs groups, along with a simulation of the ulcer healing process. Scale bar: 1 mm. **b** Quantitative analysis of the area of remaining unhealed ulcers at the time of rat execution. **c** Quantitative analysis of daily ulcer healing

patches. Using a random group design, the rats were divided into a control group and four treatment groups: HA MNs, EPL MNs, MC MNs, and HEMC MNs. The effects of the different intervention methods on ulcer healing were evaluated (Fig. 8a). The results of the study showed that the MC MNs and HEMC MNs groups significantly accelerated the wound healing process, and the HEMC MNs group performed particularly well (Fig. 8b, c). On the fifth day of treatment, the rats showed bright mucosal color and significantly enhanced healing.

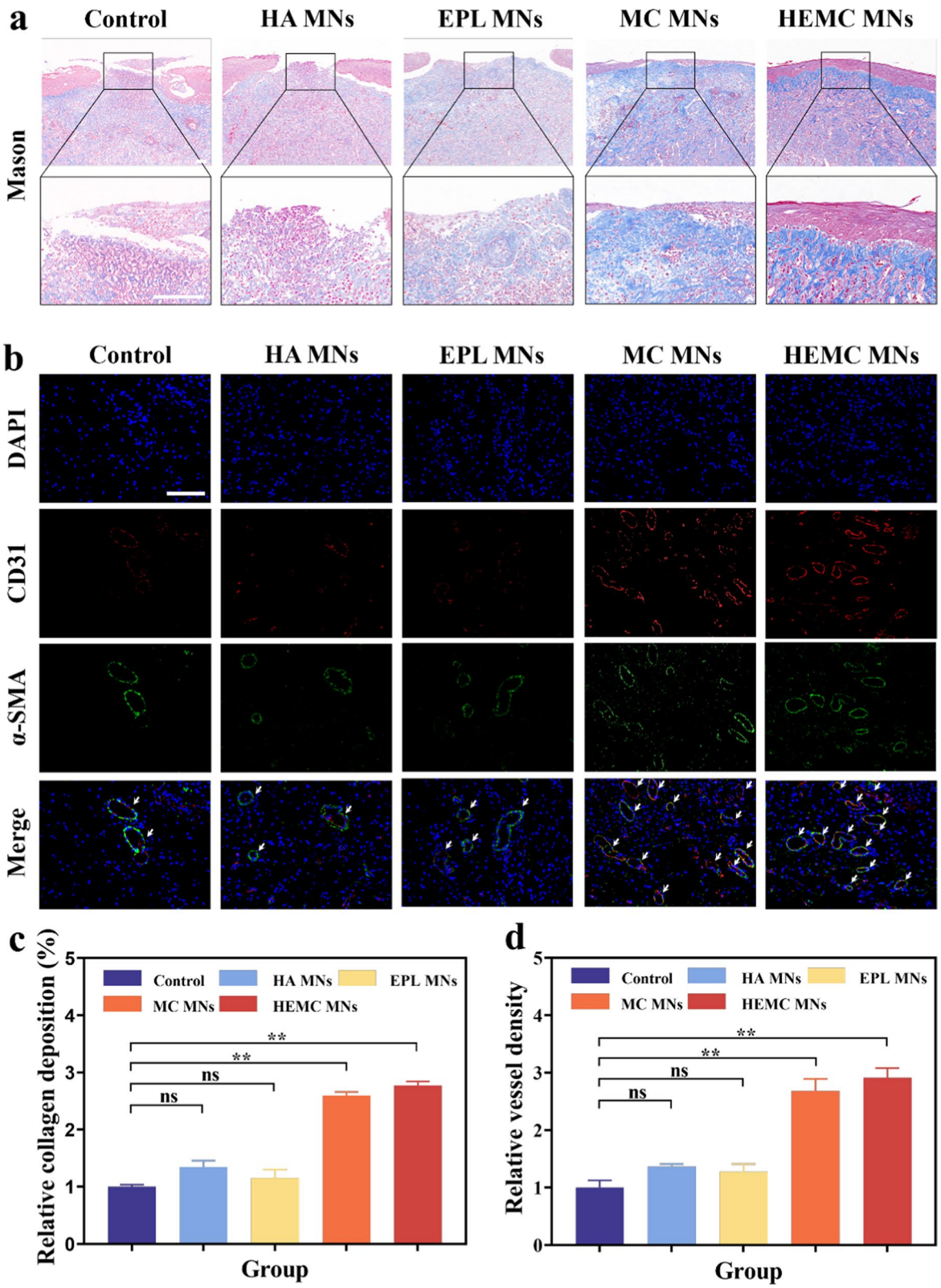

Fig. 9 Study on collagen deposition and angiogenesis after MNs treatment. **a** Microscopic images of mucosal tissues following treatment in different MNs groups, stained using Masson trichrome. Scale bar: 100 μm. **b** Fluorescence micrographs of double immunofluorescence staining for vascular endothelial cell marker CD31 (red) and vascular smooth muscle cell marker α-SMA (green). Scale bar: 100 μm. **c** Quantitative analysis of collagen deposition in ulcerated tissue. **d** Quantitative analysis of neovascularisation in tissues

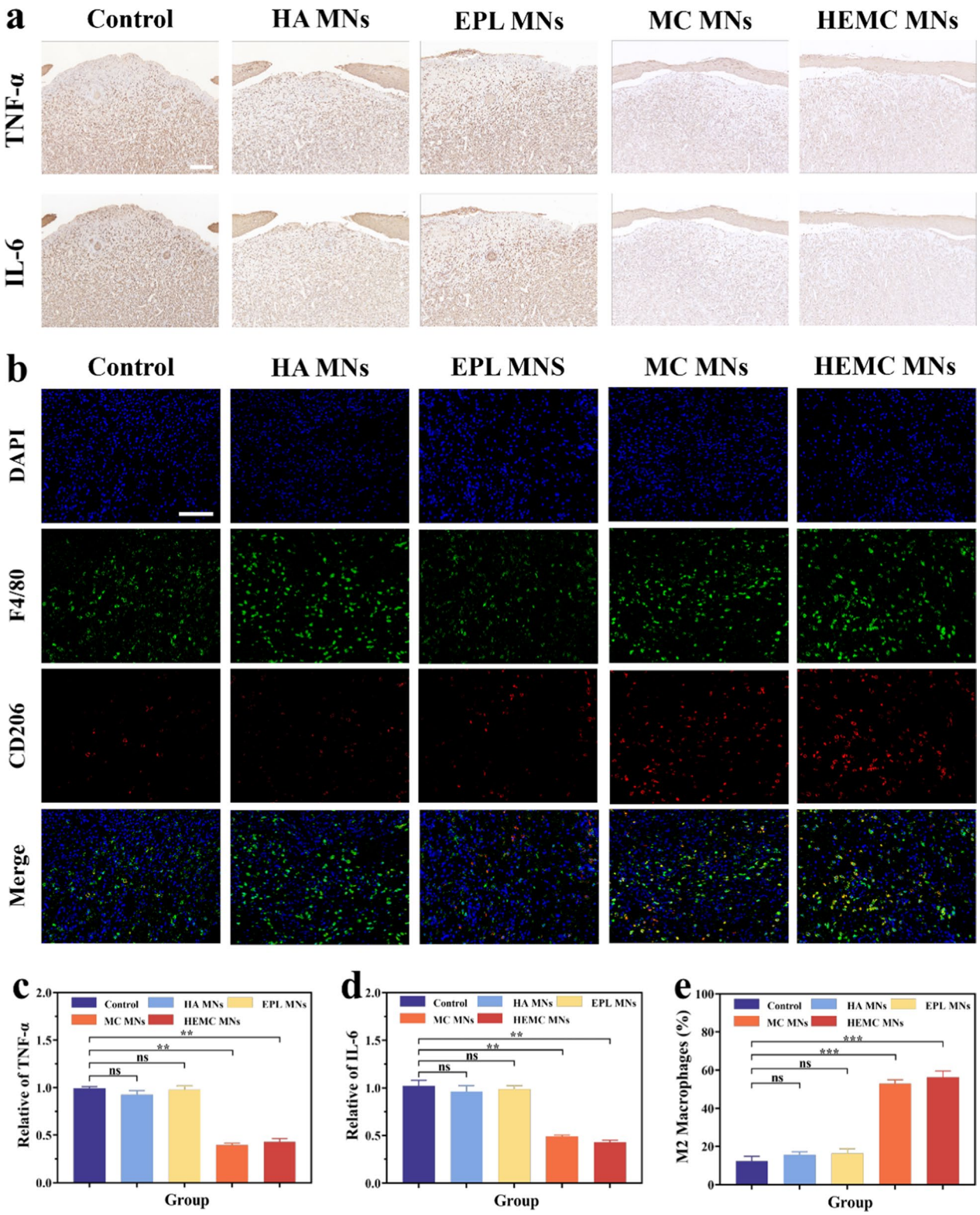

Fig. 10 Research on inflammatory factors and macrophage polarization in ulcers. **a** Immunohistochemical analysis of TNF-α and IL-6 in ulcer tissues. Scale bar: 200 μm. **b** Fluorescent microscopy images showing F4/80 and CD206 immunofluorescence staining in ulcerated tissue. Scale bar: 100 μm. **c** IL-6 immunohistochemical staining quantitative analysis. **d** TNF-α immunohistochemical staining quantitative analysis. **e** Quantitative analysis of CD206 expression-positive M2-type macrophages

Further histological H&E staining analysis revealed that the HEMC MNs group had an excellent effect in promoting epithelial layer regeneration, optimizing connective tissue arrangement, and reducing inflammatory cell infiltration, which was significantly better than that of the control group (Figure S10). Previous academic research has confirmed that in a standardized oral ulcer rat model, it takes 6 days for traditional commercial triamcinolone acetonide oral ointment to achieve a wound healing rate of approximately 80% [33]. We constructed five additional groups of oral ulcer rat models to verify further the therapeutic effect of HEMC MNs on oral ulcers. One group was set as a blank control without any intervention. The other three groups were treated with triamcinolone acetonide ointment, propolis oral film, and dexamethasone ointment which are currently widely used in clinical practice, and the last group was treated with HEMC MNs (Figure S11a). The results of the study show that all four treatment groups can effectively accelerate the healing process of oral ulcers. It is particularly noteworthy that among the four treatment groups, the HEMC MNs group showed significant pro-healing advantages, increasing the wound healing rate to nearly 90% in just five days and significantly optimizing the mucosal morphology (Figure S11b, c). As oral ulcer lesions are often accompanied by the formation of pseudomembranes, which constitute a physical barrier to drug penetration, traditional ointment formulations have difficulty adhering closely to the lesion area and are easily affected by saliva washout; therefore, their efficacy is limited. Owing to their unique penetrating ability, HEMC MNs can effectively deliver drugs to deep mucosal tissues to achieve a more stable and in-depth therapeutic effect, thus providing a new strategy to solve the above problems. This finding not only verifies the role of HEMC MNs in the innovative efficacy of promoting the healing of oral ulcers but also provides a solid experimental foundation for the development of precision medicine strategies.

We systematically evaluated collagen deposition and angiogenesis during the healing process of oral ulcers in each experimental group to comprehensively analyze its tissue remodeling mechanism. The results showed that the MC MNs and HEMC MNs groups showed significant advantages in promoting collagen deposition, especially the HEMC MNs group, whose significant collagen enrichment effect demonstrated its unique innovation in promoting tissue matrix remodeling (Fig. 9a,c). Furthermore, by accurately analyzing the expression of CD31 and α-SMA using double immunofluorescence staining, we explored the contribution of angiogenesis to tissue repair (Fig. 9b). The study found that the control group had sparse vascular structure and low expression of CD31 and α-SMA, while the MC MNs and HEMC MNs groups showed significant signs of angiogenesis, especially the HEMC MNs group, which not only effectively reduced the inflammatory response, but also significantly increased the expression of vascular markers and promoted the formation of new blood vessels (Fig. 9d). It is worth noting that the synergistic effect of Mg-MOF and CUR in MC further accelerates this process, highlighting the great potential of innovative treatment strategies based on HEMC MNs patches to accelerate angiogenesis and promote the comprehensive repair of ulcer tissue.

Inflammation is a critical marker of the progression of wound healing. To investigate this, the levels of TNF-α and IL-6 were assessed using immunohistochemical analysis on day 5 (Fig. 10a). We observed significant expression of TNF-α and IL-6 in the control group (Fig. 10c, d). Conversely, the levels of TNF-α and IL-6 were reduced in the groups treated with MC and HEMC MNs because of the effective modulation of the aberrant immune response in ulcers by the release of CUR, which resulted in decreased levels of pro-inflammatory cytokines. To evaluate the degree of inflammation at the wound site, macrophage infiltration was examined using immunofluorescence staining, with CD206 as a representative surface marker for M2 macrophages (Fig. 10b). Both the MC and HEMC MNs groups demonstrated an increase in the proportion of CD206-positive macrophages compared to that in the control group (Fig. 10e). This outcome indicates that HEMC MNs have the potential to induce macrophage polarization toward the M2 phenotype, leading to a decrease in inflammation and a transition in the local tissue environment from pro-inflammatory to pro-reparative mechanisms. Collagen deposition, increased neovascularization, and anti-inflammatory properties all indicate the potential advantages of HEMC MNs patches in wound healing.

Conclusion

In summary, this study innovatively developed a multifunctional HEMC MNs patch that integrates sustained drug release, diverse treatments, and natural biomaterials for the treatment of recurrent oral ulcers. This study is the first to use a bioactive magnesium-based metal–organic framework to load the natural biomaterial CUR to treat oral mucosal diseases. It achieves slow release of the drug and gradual decomposition of MC nanoparticles, significantly improving treatment efficiency. This design integrates multiple treatment strategies, not only showing excellent biocompatibility, hygroscopicity, and biodegradability, but also having rapid antibacterial and anti-inflammatory properties, effectively regulating the ulcer microenvironment, reducing inflammatory infiltration, promoting collagen deposition, promoting the

transformation of macrophage pro-repair phenotype, and accelerating vascular regeneration. The results highlight the efficiency and potential of HEMC MNs patches in the treatment of recurrent oral ulcers, open up a new research direction in the field of oral disease treatment, and provide a valuable theoretical and practical basis for subsequent research.

This study demonstrated that HEMC MNs have great therapeutic potential in the field of oral medicine and have provided valuable preliminary data for the treatment of oral ulcers through animal experiments. However, the complexity of the human oral environment may affect the efficacy of the MNs patches. More experiments are needed to verify its long-term stability in clinical settings, and its efficacy should be further verified in clinical trials. In addition, the current exploration of the cause of oral ulcers remains unclear. In the future, genomics, proteomics, and other technologies should be combined to explore the mechanism of MNs in the treatment of oral ulcers and to provide a theoretical basis for precision medicine. Finally, the way in which MNs play a role in the lesion site can be further expanded, and MNs can be designed into stimulus-responsive MNs to sense the dynamically changing microenvironment of the oral cavity, achieve spatiotemporal controlled release of drugs, and provide a more intelligent and efficient treatment method in the field of oral medicine.

Materials and methods

Materials

$MgCl_2$, gallic acid, HA, EPL, and CUR were purchased from Aladdin Biochemical Technology Co. Ltd. (Shanghai, China). The PDMS molds were purchased from Shiling Laker Mold Merchant (Guangzhou, China). We purchased DMSO from Sigma-Aldrich (St. Louis, MO). The Calcein/PI Cell Viability/Cytotoxicity Assay Kit, Total Antioxidant Capacity Assay Kit with ABTS, Reactive Oxygen Species Assay Kit, and Cell Counting Kit-8 (CCK-8) were purchased from Beyotime (China). The DPPH Free Radical Scavenging Capacity Assay Kit was purchased from Solebao Technology Co., Ltd. (Beijing, China). Matrigel was purchased from CORNING (Shanghai, China). Anti-CD86, Anti-CD206, and Goat Anti-Rabbit IgG H&L antibodies were purchased from Abcam (Shanghai, China).

Cell and animal cultures

Cell lines were purchased from OriCell (Shanghai, China). Sprague–Dawley (SD) rats (8 weeks old) were obtained from Hunan Slack Jingda Experimental Animal Co., Ltd. (Changsha, China) were raised in a specific pathogen-free environment. The animal experiments were approved by the research ethics committee (Approval Number: DWSY-2024–002).

Fabrication of Mg-MOF and CUR-loaded Mg-MOF

Mg-MOF was prepared using a hydrothermal synthesis technique. Water (50 mL), 1 g $MgCl_2$ and 3.8 g gallic acid were mixed, stirred under reflux, adjusted to pH 8, and heated at 140 °C in a muffle furnace (Bona Re New Materials Technology Co., Ltd., Tianjin, China) for 24 h. Subsequently, CUR was dissolved in ethanol, ultrasonically treated, and then mixed and stirred with Mg-MOF for 24 h. Mg-MOF particles loaded with CUR were obtained after centrifugal washing. Finally, the concentration of the MC solution was determined using UV spectrophotometry combined with a standard curve. The drug-loading capacity and encapsulation efficiency were quantified by applying the following mathematical expressions:

$$\text{Loading capacity}(\%) = \frac{M0 - M1}{M + (M0 - M1)} \times 100\% \quad (1)$$

$$\text{Encapsulation efficiency}(\%) = \frac{M0 - M1}{M0} \times 100\% \quad (2)$$

In this context, M denotes the mass of the Mg-MOF, while M0 and M1 signify the overall mass of the encapsulated and non-encapsulated CUR, respectively.

MNs patch preparation

HEMC MNs were prepared by a two-step casting method: first, MC was dissolved in DMSO, diluted with PBS, and then mixed with HA powder and cross-linked using 1,4-butanediol diglycidyl ether (BDDE) to form a hydrogel; EPL-loaded HA hydrogel was prepared in the same way. Next, the MC-loaded HA hydrogel was placed in a PDMS mold and the tip was filled under vacuum to promote tip filling. After removing the excess solution, EPL-loaded HA hydrogel was added under the same conditions to form a backing layer. Each HEMC MNs contained approximately 71.4 μg ml^{-1} of MC and 200 μg/ml of EPL.

Characterization of the MOFs and MNs

Bright-field images were acquired and recorded using a stereomicroscope (Leica M165C, Germany), whereas MNs patches and MC particles were imaged using scanning electron microscopy (Regulus 8100, HITACHI, Japan). The elemental composition of the MC nanoparticles was analyzed using EDS (AZtecLive Ultim Max 100, UK). The characteristic peaks of Mg-MOF, CUR, and MC were observed using FT-IR spectroscopy. The crystal structures of the samples were analyzed using XRD. The UV–vis (PE lambda 750, USA) spectrum of Mg-MOF was acquired through spectrophotometric analysis. The zeta potentials of Mg-MOF and MC were assessed using dynamic light scattering. The particle size distributions

of Mg-MOF and MC were analyzed using a laser particle size analyzer. HEMC-MNs were placed in PBS to monitor the release of Mg-MOF and CUR. The absorbance of the supernatant was regularly sampled and analyzed, and the released concentration was determined based on a calibration curve.

Hygroscopicity test

The desiccated MNs patches were stored in an airtight container at 75% humidity. MNs were extracted at 5-min intervals, photographed, and recorded using a stereomicroscope.

MNs adhesion strength test experiment

To evaluate the adhesion strength of MNs, a lap shear test was performed using a universal testing machine (MTS Insight, MTS, USA). The test samples were pig buccal mucosa obtained from a slaughterhouse, which was cut in a standardized manner and placed on both sides of the MNs to simulate the actual application scenario. Adhesion strength (kPa) was determined by dividing the load by the bonding area.

Cytotoxicity test

The cytotoxicity of MC, EPL, and MNs was evaluated using the CCK-8 test and live-dead cell staining. MNs were immersed in serum-containing medium to prepare extracts, and HUVECs were seeded in 96-well plates and exposed to different concentrations of the MC, EPL, and MNs extracts for 24 h. Cell viability was evaluated using the CCK-8 reagent, and the live-dead cell ratio was observed using calcein and propidium iodide staining combined with fluorescence microscopy to comprehensively evaluate the biocompatibility of the material.

Hemolysis test

Following isoflurane anesthesia, periorbital venous blood was collected from the SD rats. The collected blood was diluted with physiological saline and centrifuged for 5 min. This centrifugation process was repeated thrice. Red blood cells were separated and prepared in a 5% solution. A positive control was prepared by mixing water with the solution and a negative control was created by mixing saline with the solution. The remaining groups were assessed using 500 μL of the MNs extract, and hemolysis was observed after incubation for 4 h at 37 °C. The absorbance of the supernatant was measured using a spectrophotometer at a wavelength of 545 nm to determine the hemolysis rate.

Scratch test

The effectiveness of the HEMC MNs in enhancing cell migration and tissue regeneration was evaluated through in vitro experiments using a cell scratch assay. The HUVEC were suspended and seeded into six-well plates, where they were cultured until they reached a cell density of approximately 90%. A linear scratch was created in the middle of each well using a 200-μL pipette tip to mimic a wound, followed by three washes with PBS. Subsequently, the cells were exposed to either normal serum-free medium (control) or medium supplemented with extracts of HA, EPL, MC, and HEMC MNs for 24 h. Photographic recordings were captured using a microscope at both 0-h and 24-h time points during co-culture to measure the degree of gap closure.

DPPH radical scavenging assessment

Mixtures of DPPH and MC solutions at varying concentrations were prepared in a 96-well plate and incubated at 37 °C for 30 min. The absorbance of the resultant solution was assessed at a wavelength of 517 nm, and the inhibition rate was determined according to the provided guidelines.

ABTS free radical scavenging evaluation

The ability of the MC solution to scavenge ABTS free radicals was tested using a detection kit. ABTS working solution was prepared according to the manufacturer's instructions. MC solutions of various concentrations (10, 20, 30, 40, 50, 60, and 120 μg mL^{-1}), as well as different MNs extracts, were added to the prepared solutions (200 μL) and incubated at 37 °C for 30 min. The absorbance of each group was quantified at 734 nm using a microplate reader (BioTek Epoch, USA), and the inhibition rate of the samples for ABST was determined according to the provided guidelines.

ROS removal experiment

The DCFH-DA probe detected the elimination of ROS in the HEMC MNs extracts. HUVECs were treated with extracts from the various MNs groups in a six-well plate for 24 h, followed by exposure to 2 mM hydrogen peroxide for 30 min. The control group consisted of untreated cells. The supernatant was removed by aspiration, and serum-free DMEM supplemented with DCFH-DA was added to the sample, which was then incubated for 20 min. The cells were then rinsed thrice with serum-free DMEM. Cell fluorescence was visualized using an inverted fluorescence microscope.

Endothelial cell tube formation assay

The ability of MC to promote angiogenesis was confirmed using blood vessel formation experiments. Matrigel was combined with serum-free DMEM at a temperature of 4 °C, introduced into a pre-chilled 96-well plate, and subjected to a 1 h incubation period. The HUVECs were

digested and resuspended in media containing different MNs extracts, and the cell suspension was seeded onto Matrigel and incubated for 4 h. Endothelial cell tubule formation was examined by microscopic observation, followed by image capture and subsequent analysis to quantify the number of nodes.

Bacterial coating tests

Antibacterial experiments were conducted using two characteristic bacterial strains, *E. coli* and *S. aureus*. Initially, specified quantities of either *E. coli* or *S. aureus* strains were inoculated into LB broth and incubated for 6 h. The bacterial suspension was subsequently diluted and combined with the MNs extract, followed by incubation for 6–8 h. The resulting mixture was evenly distributed on a plate and incubated for 12 h.

The bacterial suspension of the blank group was incubated with the extracts of HA, EPL, MC, and HEMC MNs, and then seeded into six-well plates. Cell spreads were cultured in six-well plates and exposed to bacterial suspensions in a bacterial incubator for > 12 h. The bacterial adherents were subsequently exposed to a 2.5% glutaraldehyde solution for 8 h, rinsed with PBS, dehydrated using ethanol, and immersed in tert-butyl alcohol prior to mounting on slides.

The antimicrobial effectiveness of the various groups of MNs was evaluated through a live–dead staining assay, using a staining solution with a concentration of 1 μL of stain per 100 μL of bacterial solution to distinguish between live and dead bacteria. Following incubation at 37 °C for 20 min, the bacterial specimens were imaged and examined using a fluorescence microscope.

ELISA experiments in vitro

The inflammation model was developed by incubating RAW264.7 macrophages in 96-well plates and pretreating them with 1 μg mL^{-1} LPS for 12 h. Subsequently, the macrophage inflammation model was exposed to extracts from various MNs groups for 24 h, and the supernatant was harvested for measurement of TNF-α/IL-6 levels using an ELISA kit, according to the manufacturer's protocol.

Immunofluorescence analysis

RAW264.7 cells were stimulated to polarize towards the M1 phenotype using 1 μg mL^{-1} LPS, followed by treatment with a culture medium containing extracts from the various MNs groups for 24 h. Following fixation in 4% paraformaldehyde for 30 min, cells were washed thrice with PBS and blocked with 5% BSA for 1 h. The cells were incubated with Anti-CD86 (1:100) and Anti-CD206 (1:100) antibodies overnight at 4 °C. The cells were then washed thrice with PBST, incubated with fluorescent secondary antibodies at room temperature, and shielded from light. The cells were then stained with DAPI in the dark and washed thrice with PBST. Finally, stained cells were examined under an inverted fluorescence microscope.

Construction of the rat model and treatment of oral ulcers in rats

The animal model used was based on the traditional method of inducing oral ulcers. After one week of adaptation, 8-week-old male SD rats were anesthetized with a cotton ball containing 50% glacial acetic acid to create an ulcer with a diameter of 5 mm on the oral mucosa. After 48 h, the rats were randomly divided into five groups (n = 5). The control group was not treated, and the experimental groups (HA, EPL, MC, and HEMC MNs) received a single MNs patch treatment on the first day of the ulcer, and pressure was applied after attachment to ensure adhesion. Changes in the ulcer were monitored daily, and the wound area and healing rate from day 0 to day 5 were evaluated.

Histological analysis

Following euthanasia, oral ulcer tissues were collected from the oral cavity of rats and subjected to staining with H&E and Masson's trichrome following a series of treatments to evaluate epithelial morphology and collagen accumulation. Subsequently, immunohistochemical staining was utilized to assess the expression of TNF-α and IL-6 and evaluate the inflammatory status of the ulcerated tissues. Immunofluorescence staining for CD31 and α-SMA markers was employed to observe angiogenesis, whereas immunofluorescence staining for F4/80 and CD206 markers was conducted to detect macrophage polarization.

Statistical analysis

Data were collected from a minimum of three experiments and are presented as the mean ± standard deviation (SD). Statistical analysis was conducted using GraphPad and ImageJ software, with unpaired two-tailed Student's t-tests for pairwise comparisons and one-way ANOVA for significance testing. Statistical significance was defined as nonsignificant (ns) for $p > 0.05$, $^{*}p < 0.05$, $^{**}p < 0.01$, and $^{***}p < 0.001$.

Supplementary Information

The online version contains supplementary material available at https://doi.org/10.1186/s12951-024-02873-y.

Supplementary Material 1.

Author contributions
L.J. Lei and M.H. Dai conceived the conceptualization and designed the experiment. J.H. Liu carried out the experiments. Z.P. Zhang, X.F. Lin, J. Hu, X.Y. Pan, A.Q. Jin and J.H. Liu participated in data analysis and discussion. J.H. Liu, L.J. Lei and M.H. Dai wrote the paper.

Funding
This work was supported by the Zhejiang Shuren University research projects (2023R053 and 2023KJ237) and the Wenzhou Science and Technology Project of China (No. Y20240232).

Availability of data and materials
No datasets were generated or analysed during the current study.

Declarations

Ethics approval and consent to participate
All animal experiments were approved by the Experimental Animal Ethics Committee of the Third Affiliated Hospital of Wenzhou Medical University (DWSY-2024-002).

Consent for publication
All authors agree to be published.

Competing interests
The authors declare no competing interests.

Author details
[1]Key Laboratory of Artificial Organs and Computational Medicine in Zhejiang Province, Institute of Translational Medicine, Zhejiang Shuren University, Hangzhou 310015, China. [2]The Third Affiliated Hospital of Wenzhou Medical University, Wenzhou 325200, China. [3]School of Chemistry, South China Normal University, Guangzhou 510631, China.

Received: 9 July 2024 Accepted: 25 September 2024
Published online: 30 September 2024

References

1. Zhang W, Bao B, Jiang F, Zhang Y, Zhou R, Lu Y, Lin S, Lin Q, Jiang X, Zhu L. Promoting oral mucosal wound healing with a hydrogel adhesive based on a phototriggered S-nitrosylation coupling reaction. Adv Mater. 2021;33(48):2105667.
2. Dudding T, Haworth S, Lind PA, Sathirapongsasuti JF, Tung JY, Mitchell R, Colodro-Conde L, Medland SE, Gordon S. Genome wide analysis for mouth ulcers identifies associations at immune regulatory loci. Nat Commun. 2019;10(1):1052.
3. Zeng X, Jin X, Zhong L, Zhou G, Zhong M, Wang W, Fan Y, Liu Q, Qi X, Guan X. Difficult and complicated oral ulceration: an expert consensus guideline for diagnosis. Int J Oral Sci. 2022;14(1):28.
4. Bilodeau EA, Lalla RV. Recurrent oral ulceration: Etiology, classification, management, and diagnostic algorithm. Periodontol 2000. 2019;80(1):49–60.
5. Patel VF, Liu F, Brown MB. Advances in oral transmucosal drug delivery. J Control Release. 2011;153(2):106–16.
6. Grennan D, Wang S. Steroid side effects. JAMA. 2019;322(3):282–282.
7. Lamont RJ, Koo H, Hajishengallis G. The oral microbiota: dynamic communities and host interactions. Nat Rev Microbiol. 2018;16(12):745–59.
8. Hearnden V, Sankar V, Hull K, Juras DV, Greenberg M, Kerr AR, Lockhart PB, Patton LL, Porter S, Thornhill MH. New developments and opportunities in oral mucosal drug delivery for local and systemic disease. Adv Drug Delivery Rev. 2012;64(1):16–28.
9. Moutsopoulos NM, Konkel JE. Tissue-specific immunity at the oral mucosal barrier. Trends Immunol. 2018;39(4):276–87.
10. Zhang Z, Zhang Q, Gao S, Xu H, Guo J, Yan F. Antibacterial, anti-inflammatory and wet-adhesive poly (ionic liquid)-based oral patch for the treatment of oral ulcers with bacterial infection. Acta Biomater. 2023;166:254–65.
11. Toma AI, Fuller JM, Willett NJ, Goudy SL. Oral wound healing models and emerging regenerative therapies. Transl Res. 2021;236:17–34.
12. Iglesias-Bartolome R, Uchiyama A, Molinolo AA, Abusleme L, Brooks SR, Callejas-Valera JL, Edwards D, Doci C, Asselin-Labat M-L, Onaitis MW. Transcriptional signature primes human oral mucosa for rapid wound healing. Sci Transl Med. 2018;10(451):eaap8798.
13. Urošević M, Nikolić L, Gajić I, Nikolić V, Dinić A, Miljković V. Curcumin: Biological activities and modern pharmaceutical forms. Antibiotics. 2022;11(2):135.
14. Yang J, Yang B, Shi J. A nanomedicine-enabled ion-exchange strategy for enhancing curcumin-based rheumatoid arthritis therapy. Angew Chem Int Ed. 2023;62(44): e202310061.
15. Huminiecki L, Horbańczuk J, Atanasov A. The functional genomic studies of curcumin. Semin Cancer Biol. 2017;46:107–18.
16. Li H, Sureda A, Devkota HP, Pittalà V, Barreca D, Silva AS, Tewari D, Xu S, Nabavi SM. Curcumin, the golden spice in treating cardiovascular diseases. Biotechnol Adv. 2020;38: 107343.
17. Yao H, Wang F, Chong H, Wang J, Bai Y, Du M, Yuan X, Yang X, Wu M, Li Y. A curcumin-modified coordination polymers with ROS scavenging and macrophage phenotype regulating properties for efficient ulcerative colitis treatment. Adv Sci (Weinheim, Ger). 2023;10(19):2300601.
18. Kocaadam B, Şanlier N. Curcumin, an active component of turmeric (*Curcuma longa*), and its effects on health. Crit Rev Food Sci Nutr. 2017;57(13):2889–95.
19. Pourhajibagher M, Hodjat M, Bahador A. Sonodynamic excitation of nanomicelle curcumin for eradication of *Streptococcus mutans* under sonodynamic antimicrobial chemotherapy: enhanced anti-caries activity of nanomicelle curcumin. Photodiagn Photodyn Ther. 2020;30: 101780.
20. Hou X, Lin H, Zhou X, Cheng Z, Li Y, Liu X, Zhao F, Zhu Y, Zhang P, Chen D. Novel dual ROS-sensitive and CD44 receptor targeting nanomicelles based on oligomeric hyaluronic acid for the efficient therapy of atherosclerosis. Carbohydr Polym. 2020;232: 115787.
21. Ganugula R, Arora M, Dwivedi S, Chandrashekar D, Varambally S, Scott E, Kumar MR. Systemic anti-inflammatory therapy aided by curcumin-laden double-headed nanoparticles combined with injectable long-acting insulin in a rodent model of diabetes eye disease. ACS Nano. 2023;17(7):6857–74.
22. Rahiman N, Markina YV, Kesharwani P, Johnston TP, Sahebkar A. Curcumin-based nanotechnology approaches and therapeutics in restoration of autoimmune diseases. J Controlled Release. 2022;348:264–86.
23. Sun L, Liu Z, Wang L, Cun D, Tong HH, Yan R, Chen X, Wang R, Zheng Y. Enhanced topical penetration, system exposure and anti-psoriasis activity of two particle-sized, curcumin-loaded PLGA nanoparticles in hydrogel. J Control Release. 2017;254:44–54.
24. Zhu X, Yu Z, Feng L, Deng L, Fang Z, Liu Z, Li Y, Wu X, Qin L, Guo R. Chitosan-based nanoparticle co-delivery of docetaxel and curcumin ameliorates anti-tumor chemoimmunotherapy in lung cancer. Carbohydr Polym. 2021;268: 118237.
25. Zhou Z, Vázquez-González M, Willner I. Stimuli-responsive metal–organic framework nanoparticles for controlled drug delivery and medical applications. Chem Soc Rev. 2021;50(7):4541–63.
26. He S, Wu L, Li X, Sun H, Xiong T, Liu J, Huang C, Xu H, Sun H, Chen W. Metal-organic frameworks for advanced drug delivery. Acta Pharm Sin B. 2021;11(8):2362–95.
27. Kang Y, Xu C, Dong X, Qi M, Jiang D. Exosome-functionalized magnesium-organic framework-based scaffolds with osteogenic, angiogenic and anti-inflammatory properties for accelerated bone regeneration. Bioact Mater. 2022;18:26–41.
28. Yang L, Li W, Zhao Y, Shang L. Magnetic polysaccharide mesenchymal stem cells exosomes delivery microcarriers for synergistic therapy of osteoarthritis. ACS Nano. 2024;18:20101–10.
29. Lyu S, Dong Z, Xu X, Bei H-P, Yuen H-Y, Cheung C-WJ, Wong M-S, He Y, Zhao X. Going below and beyond the surface: microneedle structure, materials, drugs, fabrication, and applications for wound healing and tissue regeneration. Bioact Mater. 2023;27:303–26.
30. Xu J, Xu D, Xuan X, He H. Advances of microneedles in biomedical applications. Molecules. 2021;26(19):5912.
31. Ge W, Gao Y, He L, Zeng Y, Liu J, Yu Y, Xie X. R-a Xu, Combination therapy using multifunctional dissolvable hyaluronic acid microneedles for oral ulcers. Int J Biol Macromol. 2023;251: 126333.

32. Zhang X, Hasani-Sadrabadi MM, Zarubova J, Dashtimighadam E, Haghniaz R, Khademhosseini A, Butte MJ, Moshaverinia A, Aghaloo T, Li S. Immunomodulatory microneedle patch for periodontal tissue regeneration. Matter. 2022;5(2):666–82.
33. Guo X, Zhu T, Yu X, Yi X, Li L, Qu X, Zhang Z, Hao Y, Wang W. Betamethasone-loaded dissolvable microneedle patch for oral ulcer treatment. Colloids Surf B. 2023;222: 113100.
34. Li Y, Bi D, Hu Z, Yang Y, Liu Y, Leung WK. Hydrogel-forming microneedles with applications in oral diseases management. Materials. 2023;16(13):4805.
35. Wang Y, Luo T, Li Y, Wang A, Wang D, Bao JL, Mohanty U, Tsung C-K. Molecular-level insights into selective transport of Mg2+ in metal-organic frameworks. ACS Appl Mater Inter. 2021;13(44):51974–87.
36. Cooper L, Hidalgo T, Gorman M, Lozano-Fernández T, Simón-Vázquez R, Olivier C, Guillou N, Serre C, Martineau C, Taulelle F. A biocompatible porous Mg-gallate metal–organic framework as an antioxidant carrier. Commun. 2015;51(27):5848–51.
37. Sardaro N, Della Vella F, Incalza MA, Di Stasio D, Lucchese A, Contaldo M, Laudadio C, Petruzzi M. Oxidative stress and oral mucosal diseases: an overview. In Vivo. 2019;33(2):289–96.
38. Gomes MS, Lins RDAU, Langassner SMZ, da Silveira ÉJD, de Carvalho TG, de Sousa Lopes MLD, de Souza Araújo AL, de Medeiros CACX, de Carvalho Leitao RF, Guerra GCB. Anti-inflammatory and antioxidant activity of hydroethanolic extract of *Spondias mombin* leaf in an oral mucositis experimental model. Arch Oral Biol. 2020;111: 104664.
39. Sun X, Jia P, Zhang H, Dong M, Wang J, Li L, Bu T, Wang X, Wang L, Lu Q. Green regenerative hydrogel wound dressing functionalized by natural drug-food homologous small molecule self-assembled nanospheres. Adv Funct Mater. 2022;32(7):2106572.
40. Wei L, Wu S, Shi W, Aldrich AL, Kielian T, Carlson MA, Sun R, Qin X, Duan B. Large-scale and rapid preparation of nanofibrous meshes and their application for drug-loaded multilayer mucoadhesive patch fabrication for mouth ulcer treatment. ACS Appl Mater Inter. 2019;11(32):28740–51.
41. Min Z, Yang L, Hu Y, Huang R. Oral microbiota dysbiosis accelerates the development and onset of mucositis and oral ulcers. Front Microbiol. 2023;14:1061032.
42. Li R, Chen T, Pan X. Metal–organic-framework-based materials for antimicrobial applications. ACS Nano. 2021;15(3):3808–48.
43. Patil NA, Kandasubramanian B. Functionalized polylysine biomaterials for advanced medical applications: a review. Eur Polym J. 2021;146: 110248.
44. Liu S, Liu X, Ren Y, Wang P, Pu Y, Yang R, Wang X, Tan X, Ye Z, Maurizot V. Mussel-inspired dual-cross-linking hyaluronic acid/ε-polylysine hydrogel with self-healing and antibacterial properties for wound healing. ACS Appl Mater Inter. 2020;12(25):27876–88.
45. Wang R, Li J, Chen W, Xu T, Yun S, Xu Z, Xu Z, Sato T, Chi B, Xu H. A biomimetic mussel-inspired ε-poly-l-lysine hydrogel with robust tissue-anchor and anti-infection capacity. Adv Funct Mater. 2017;27(8):1604894.
46. Salehi B, Jornet PL, López EP-F, Calina D, Sharifi-Rad M, Ramírez-Alarcón K, Forman K, Fernández M, Martorell M, Setzer WN. Plant-derived bioactives in oral mucosal lesions: a key emphasis to curcumin, lycopene, chamomile, aloe vera, green tea and coffee properties. Biomolecules. 2019;9(3):106.

Publisher's Note